Effects of Yttrium and Cerium co-substitution on Structures and Magnetic Properties of Nanocrystalline Nd-Fe-B Magnets

Xiaoqiang Yu[1,2,3]*, Lei He[1], Yuting Hu[1], Jiajie Li[1,2,3]**, Xiao Liu[1], Yuhan Wang[1], Chunji Li[1], Munan Yang[1,2,3], and Zhenchen Zhong[1,2,3]

[1]*Jiangxi Key Laboratory for Rare Earth Magnetic Materials and Devices/Institute for Rare Earth Magnetic Materials and Devices, College of Rare Earths, Jiangxi University of Science and Technology, Ganzhou 341000, China*
[2]*National Rare Earth Functional Materials Innovation Center, Ganzhou 341000, China*
[3]*Key Laboratory of Development and Application of Ionic Rare Earth Resources (Jiangxi University of Science and Technology), Ministry of Education, Ganzhou 341000, China*

Cerium-containing (Ce) rare earth magnets with extraordinary cost-effectiveness are widely investigated around the world. However, when the concentration of Ce is much more, the kind of these magnets exhibits very poor thermal stability and overall magnetic properties. To weaken these disadvantages, we take eutectic $Y_{50}Ce_{50}$ co-substitution alloys into account in this work. Magnetic properties, microstructures and metallurgical behaviors of (Y, Ce, Nd)-Fe-B magnets are systematically researched. For $(Y_{50}Ce_{50})_{10}Nd_{20}Fe_{68.9}B_{1.1}$ SPSed permanent magnets, good overall magnetic properties are H_{cj} = 725 kA/m, J_r = 0.73 T and $(BH)_{max}$ = 81 kJ/m^3. It schematically depicts that coarse grain zones and fine grain zones occur during the spark plasma sintering (SPS) process. With the Nd content increasing, the deleterious $CeFe_2$ phases disappear. In addition, the volume fraction and width of coarse grain zones decrease. Ce-rich and Ce-lean regions are also observed in main phases, while Y and Nd elements are uniformly distributed. TEM results show that Nd and Ce are rich in the grain boundary and Y elements prefer to enter in 2:14:1 main phases. This work is favorable to a balanced utilization of high abundance rare earth elements in Nd-Fe-B magnets.

Keywords : Cerium-containing magnets, magnetic properties, spark plasma sintering, Nd-Fe-B

1. Introduction

It is well known to us that Nd-Fe-B permanent magnets play an important role in the field of new energy, such as hybrid vehicles and wind turbines [1-4]. Among the rare earths (RE), (Nd, Pr, Dy and Tb) medium or heavy RE elements are mainly consumed in Nd-Fe-B permanent magnets. On the contrary, the high abundant and much cheaper light RE elements (La, Ce and Y) are rarely used, which causes backlog for a long time [5].

Currently, A global advice of reducing production costs and balancing utilization of high-abundance rare earth elements has attracted much attention. Especially, the wide application of La/Ce/Y rare earth resources is emphasized. Based on the previous researches, the 2:14:1

tetragonal structure of $La_2Fe_{14}B$ is unstable and difficult to form [6], while the Ce element can completely replace Nd in $Nd_2Fe_{14}B$ phase to form analogous 2:14:1-type tetragonal phase. However, the Ce-containing magnets exhibit only moderate magnetic properties, because the intrinsic magnetic properties of $Ce_2Fe_{14}B$ (J_s = 1.17 T, H_A = 2070 kA/m) are much lower than those of $Nd_2Fe_{14}B$ (J_s = 1.60 T, H_A = 5811 kA/m). Especially, its saturation magnetization is much lower [7]. Unfortunately, the thermal stability of $Ce_2Fe_{14}B$ is far inferior to that of $Nd_2Fe_{14}B$. Therefore, many recent researches focus on the bottleneck breakthrough of Ce-containing magnets at high temperature.

Based on its similar physical and chemical properties (like Ce rare earth element), Yttrium (Y) element is generally considered to be a member in the rare earth elements family [8]. The intrinsic magnetic properties of $Y_2Fe_{14}B$ (J_s = 1.41 T, H_A = 2070 kA/m) are similar to those of $Ce_2Fe_{14}B$. Although magneto-crystalline anisotropy field (H_A) of $Y_2Fe_{14}B$ is much lower than that of

*Corresponding author: Tel: +86-797-8312151
e-mail: yuxiaoqiang@jxust.edu.cn
e-mail: lijiajie@jxust.edu.cn

$Nd_2Fe_{14}B$, the Curie temperature (T_C = 565 K) and saturation magnetization (J_s = 1.41 T) approach to those of $Nd_2Fe_{14}B$ (T_C = 585 K, J_s = 1.60 T) [7]. Moreover, proportion of Y in our planet is much higher and the price is much lower compared with Nd or Nd-Pr alloys, which suggests that Y may be a potential candidate to improve the thermal stability of Ce-containing magnets. Liao *et al.* has studied nanocrystalline $Y_2Fe_{14}B$ alloys with La or Ce substitutions and found that (Y, Ce)-Fe-B alloys have similar weak temperature dependence of anisotropic field, which can effectively improve its thermal stability of coercivity [9].

Superior magnetic performances use to depend on the excellent microstructure. It is reported that nanocrystalline Nd-Fe-B magnets have better temperature dependence of coercivity and fracture toughness as compared to conventional microcrystalline sintered magnets [10, 11]. Due to these advantages of lower heating temperature and shorter holding time, spark plasma sintering (SPS) process wakens nanocrystalline magnets in promising prospect [12-14]. Although J_s of $Y_2Fe_{14}B/Ce_2Fe_{14}B$ is relatively low, the increment overall magnetic properties of (Y, Ce, Nd)-Fe-B magnets can be obtained by means of preferential distribution of Y, Ce and Nd rare earth elements. Based on related reports, Pr-Cu diffusion/PrNd-Cu infiltration or Ce-Co additions were ever adopted to improve magnetic properties of hot-pressed or hot-deformed magnets in this way [15-17]. In spite of alloys/ribbons with higher coercivity, neither great remanence nor maximum magnetic energy product (overall magnetic properties) might be obtained. In addition, within considering their practical demands of permanent magnets, SPS process is further operated after the first as-pressing step. Microstructures of alloys and distribution behaviors of rare earth elements (Y, Ce, Nd) are very critical to magnetic properties.

In this work, we systematically study the evolution of thermal stability, microstructure and metallurgical behavior in nanocrystalline (Y, Ce, Nd)-Fe-B SPSed magnets to make rare earth elements effective and sustainable development.

2. Experimental

The ingots with the nominal composition of $(Y_{50}Ce_{50})_{30-x}Nd_xFe_{68.9}B_{1.1}$ (x = 0, 5…, 25, 30, wt.%) were marked as Nd-0, Nd-5…, Nd-25, Nd-30, respectively. Then these ingots were melt-spun onto a Cu crucible with quench wheel speed of 25-35 m/s under high-purity argon protection. Powders were obtained by grinding the ribbons. The nanocrystalline magnets were fabricated by spark plasma sintering system (LANBOX-1575F) at a high vacuum

atmosphere. The sintering temperature/holding time and pressure were in range of 600-700 °C (873-973 K)/3-5 min under 50-60 MPa. In the initial period, solid objects were prepared under lower temperature and pressure (about 300 K and 10-20 MPa). Then, with raising temperature and holding time up to the respective optimal value, as-sintered magnets were compacted to approach the densification. Meanwhile, better elongated grains in order were gained as well. Density of these samples was measured by the Archimedes Principle. The magnetic properties were tested by the Physical Property Measurement System (PPMS, Quantum Design, USA), the *M-H* curves were obtained at a maximum field of 5 T. A magnetic field of 0.1 T and temperature range of 300-650 K were applied to measure the *M-T* and d*M*/d*T* curves. Phase structure was characterized by X-ray diffraction (XRD) with Cu K_α radiation in the range of 20º-70º. The microstructural features and elements distribution were studied by the field emission scanning electron microscope (SEM/EDS, MLA 650FEI) operated under 20 kV. The grain morphology and size were tested by transmission electron microscopy (TEM, Tecnai G^2 F30).

3. Results and Discussion

The XRD patterns of Nd-0, Nd-10, Nd-20 and Nd-30 alloys are shown in Fig. 1(a). Measured XRD patterns are analyzed by the MDI Jade 6.5 software. From the diffraction peaks, both 2:14:1 (space group $P4_2$/mnm) main phases and $CeFe_2$ (space group Fd-3m) phase can be detected. Characteristic indexes of $CeFe_2$-type phases are the (220) and (311), respectively.

With the Nd content increasing, the characteristic peaks of incorporating $CeFe_2$-type Laves phases disappear and remain unique 2:14:1 main phases in Nd-20 and Nd-30 ribbons. It signifies that higher Nd content is helpful to suppress the other undesirable phases, such as $CeFe_2$-type phases. In terms of the peaks location, 2:14:1 diffraction peaks shift slightly to lower angle degree. Magnified characteristic peaks are shown in Fig. 1(b). This variation is associated with the substitution of Y and Ce for Nd in the main phase due to the smaller lattice parameters of $Y_2Fe_{14}B/Ce_2Fe_{14}B$ compared with those of $Nd_2Fe_{14}B$ at room temperature [7].

At room temperature, demagnetization curves of Nd-0 ~ Nd-30 alloys/ribbons are described in Fig. 2(a). For Nd-0 alloys, the magnetic properties of H_{cj} = 363 kA/m, J_r = 0.67 T, and $(BH)_{max}$ = 63 kJ/m^3 are obtained. With increase of Nd content, the magnetic properties are monotonously improving. For Nd-30 alloys, the highest magnetic properties are achieved, H_{cj} = 1362 kA/m, J_r = 0.76 T and
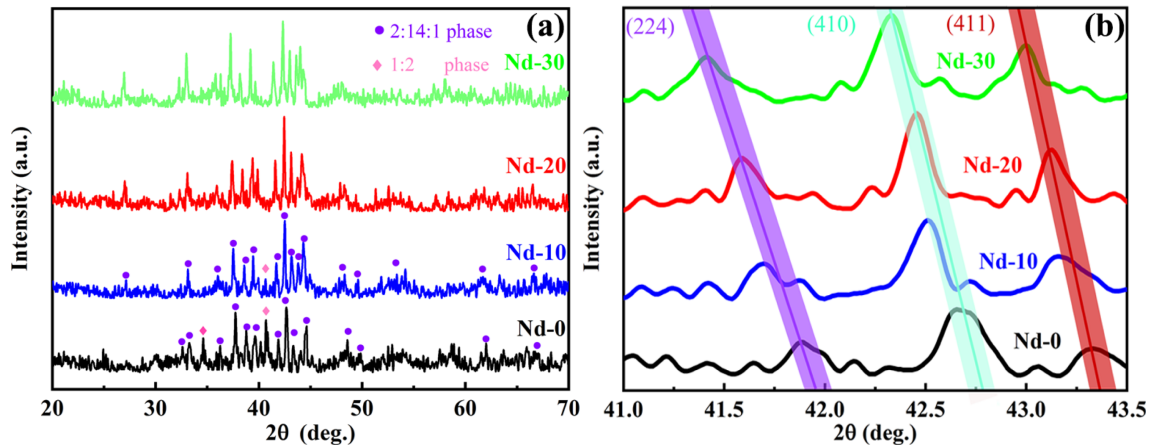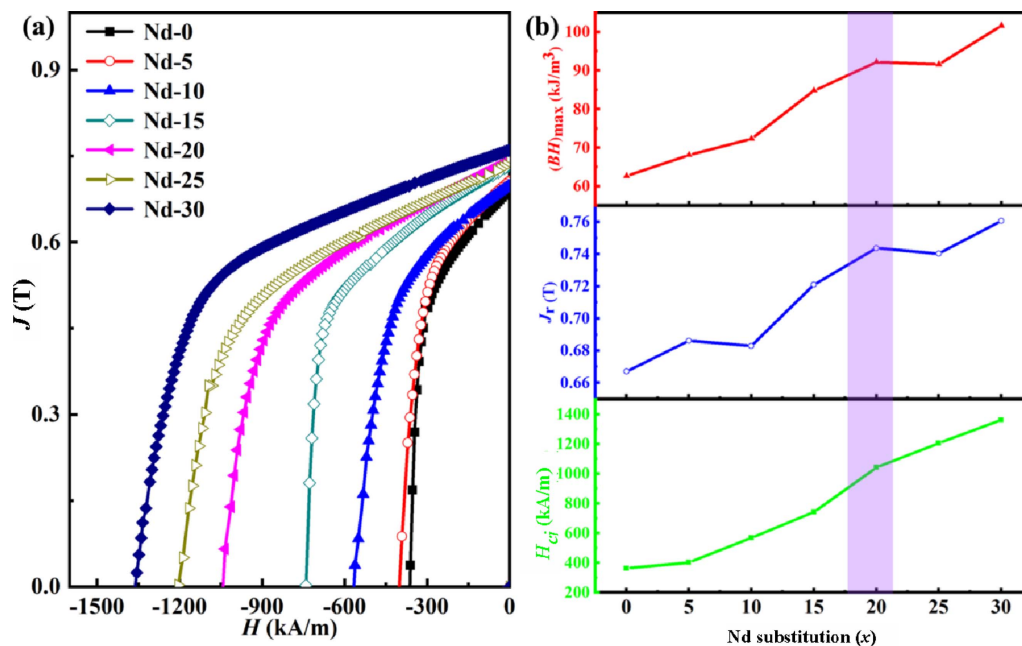
Fig. 1. (Color online) (a) The XRD patterns of Nd-0, Nd-10, Nd-20 and Nd-30 ribbons, (b) the magnified graphs in the range of 41°-43.5°.

$(BH)_{max}$ = 102 kJ/m³, respectively. The reason is ascribed to a certain relationship between intrinsic coercivity (H_{cj}) and magneto-crystalline anisotropy field (H_A). Intrinsic magnetic properties of $Nd_2Fe_{14}B$ are sufficiently superior to those of $Ce_2Fe_{14}B$ and $Y_2Fe_{14}B$ as mentioned above [7], which is the main reason for the increased coercivity. The remanence is related to the volume fraction of the main phases. Thus, a further small amount of $CeFe_2$ nonmagnetic phase is more conducive to the enhancement of remanence [18], which is agreement with the XRD results shown in Fig. 1(a).

As described in Fig. 2(b), both J_r and $(BH)_{max}$ can be improved with increasing Nd content and reach a sudden change in Nd-20 alloys with H_{cj}, J_r and $(BH)_{max}$ of 1042 kA/m, 0.74 T and 91 kJ/m³, respectively. It is worth noting that the weight ratio of $Y_{50}Ce_{50}$ alloys content is approximate 33 % of the gross rare earth elements in Nd-20 alloys. On the basis of these results given above, (Y, Ce)-containing alloys are potentially utilized to fabricate higher performance instead of cost in Nd-Fe-B permanent magnets.

Nd-0, Nd-10, Nd-20 and Nd-30 nanocrystalline alloys/ribbons are crushed into powders. These powders are fully made into starting objects. Continuously, these pre-


Fig. 2. (Color online) (a) At room temperature demagnetization curves of Nd-0, Nd-10, Nd-20 and Nd-30 ribbons and (b) variation of magnetic properties as a function of Nd substitution.
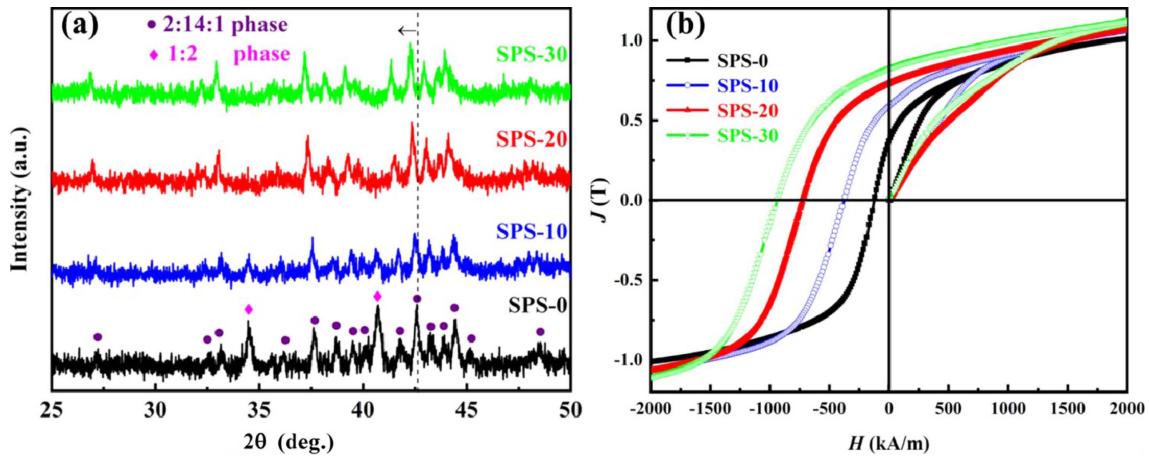
Fig. 3. (Color online) (a) XRD patterns of SPS-0 ~ SPS-30 magnets and (b) magnetization curves of SPS-0 ~ SPS-30 magnets at room temperature.

cursors are subjected to prepare as-sintered magnets/ SPSed magnets and marked as SPS-0, SPS-10, SPS-20, SPS-30, respectively. Magnetic properties of all SPSed magnets are optimized. Measured XRD patterns of SPSed magnets are exhibited in Fig. 3(a). At the same time, their optimal magnetic properties are recorded in Fig. 3(b). Interestingly, phase compositions of SPSed magnets

slightly deviate from those of respective ribbons shown in Fig. 1(a). The $CeFe_2$-type phases still do not coexist in SPS-20 and SPS-30 magnets, which indicates that $CeFe_2$-type phases do not appear at all during SPS process. Taking this SPS procedure into account, nanocrystalline permanent magnets with high purity 2:14:1 main phases can be subsequently and quickly derived after the pre-
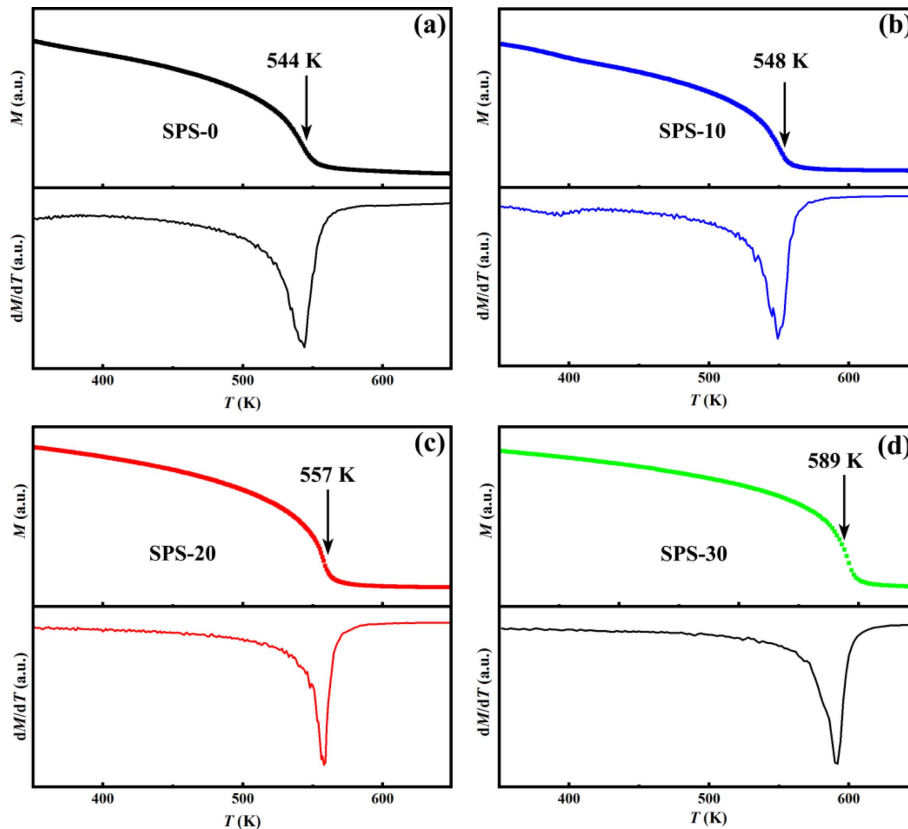
Fig. 4. (Color online) *M-T* curves and d*M*/d*T* curves of (a) SPS-0, (b) SPS-10, (c) SPS-20 and (d) SPS-30 magnets.

compacting step. It is one of critical reasons, why we adopt SPS procedure to prepare nanocrystalline samples. The melting point of $CeFe_2$ phase is 1198 K, which is much higher than that of Nd-rich phase [19]. Therefore, the existence of $CeFe_2$ phase inevitably affects the wettability of liquid phase in magnets. Curie temperature of $CeFe_2$ phase is 235 K. It shows paramagnetism at room temperature. So the $CeFe_2$ phase also dilutes the volume fraction of main phases and deteriorates overall magnetic properties [20]. The magnetization curves of these magnets are presented in Fig. 3(b). The remanence and coercivity of SPS-0 magnet are all very low, moreover, the density is very low (6.64 g/cm³). For the SPS-20 magnets, the H_{cj} = 725 kA/m, J_r = 0.73 T and $(BH)_{max}$ = 81 kJ/m³ are obtained.

Curie temperature (T_C) is an important indicator when these magnets are working at high temperature. Therefore, it is of great significance to increase the Curie temperature. M-T curves of the SPSed magnets are acquired in the temperature range of 300-650 K. The M-T curves and dM/dT curves of SPS-0, SPS-10 and SPS-20 magnets are shown in Fig. 4. It is well known that Curie temperature is sensitive to the composition of the magnets [21]. T_C of $Ce_2Fe_{14}B$ and $Y_2Fe_{14}B$ are 424 K and 565 K, respectively

[7]. With respect to SPS-0 magnet, the theoretical value is about 495 K, which is calculated by simple mathematics according to the respective weight percentage of Y and Ce. While the experimental result (T_C) of SPS-0 magnet is 544 K shown in Fig. 4(a). This value likely corresponds to that of $(Y_{85}Ce_{15})_2Fe_{14}B$ phase and may result from the different interdiffusion behaviors of Y and Ce elements. Curie temperatures of SPS-10 and SPS-20 are 548 K and 557 K, respectively. It implies that Nd/Y/Ce elements diffusing is helpful for forming the propagated (Y, Ce, Nd)-Fe-B phases and this behavior facilitates the T_C further increasing. As comparison, T_C of SPS-30 magnet is 589 K, which is almost equal to the pure/unique $Nd_2Fe_{14}B$ main phase [7]. Discovery of Nd/Y/Ce elements metallurgical diffusion behaviors holds a promising way to improve better working capability of nanocrystalline Nd-Fe-B permanent magnets at high temperature.

The overall magnetic performances of SPSed magnets are always related to the microstructural evolution. In order to study the microstructures of the magnets, the SEM images are obtained. Morphologies of SPS-0, SPS-10, SPS-20 are given in Fig. 5. For the SPS-0 magnet, it can be well discerned in Fig. 5(a) and Fig. 5(b). There a crevice exists between adjacent flakes, which intimates
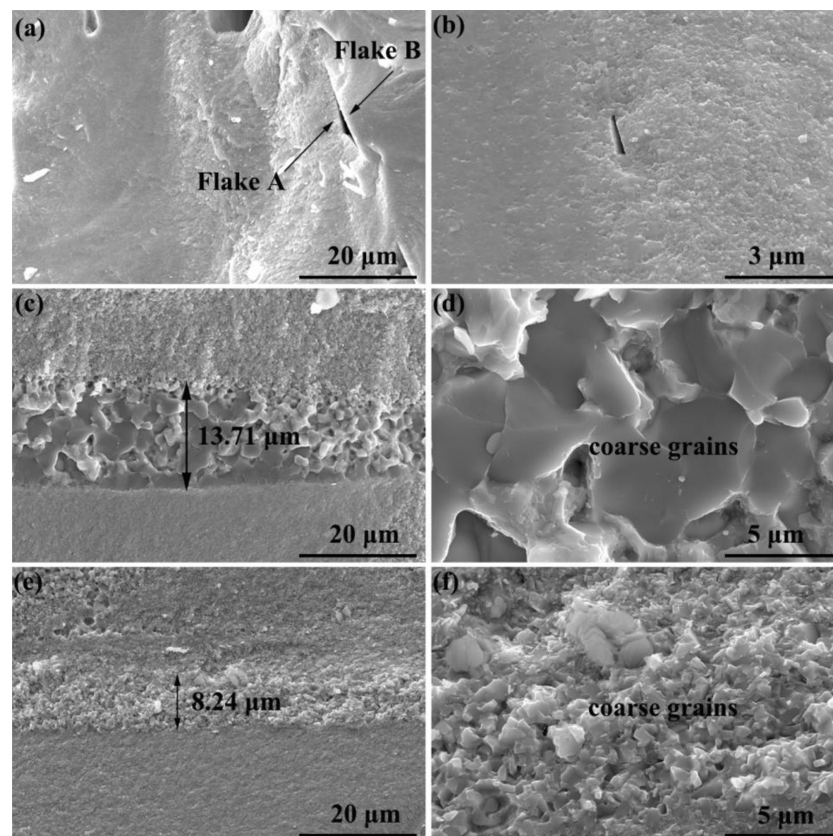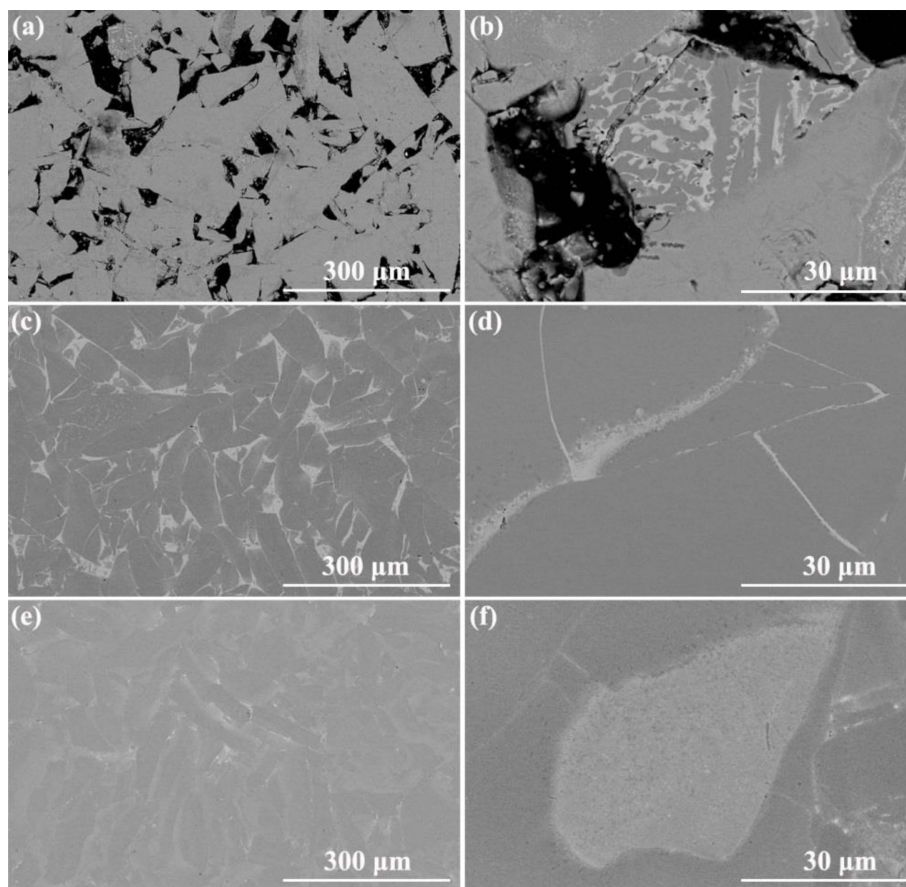

Fig. 5. SEM micrographs and magnified images of (a, b) SPS-0, (c, d) SPS-10 and (e, f) SPS-20 magnets.

Fig. 6. BSE images of (a, b) SPS-0, (c, d) SPS-10 and (e, f) SPS-20 magnets.

less liquid phases remaining in order to become the densification. The existence of $CeFe_2$ should be responsible for this result. It is reported that temperature in the particle boundary rises to about 3300 K, while temperature in the particle center is much lower than that in particle boundary during the SPS process [14]. Accompanying transient gradient field at high temperature, the coarse grain zones and fine grain zones coexist in SPSed magnets. Coarse grain zones correspond to the flake boundary. Analogously, fine grain zones correspond to the parts in particle center. With regard to SPS-10 magnet, the width of coarse grain zone is about 13.71 μm. As comparison, it declines to 8.24 μm in SPS-20 sample. The grain size and volume fraction of coarse grain zone are also decreasing with increasing Nd content shown in Fig. 5(c)-(f). It is beneficial to enhancement of the coercivity due to refining grain sizes [14, 22].

To get deeper insight into phase constitutions of SPS-0, SPS-10, SPS-20 magnets, backscattered electron images are shown in Fig. 6. A few of voids can be obviously seen in SPS-0 magnet shown in Fig. 6(a) and Fig. 6(b). The dark areas are voids. Almost condensed magnets are fabricated after the same sintering process for SPS-10 and SPS-20. Density of SPS-0 magnet is 6.64 g/cm^3, while that of SPS-10/SPS-20 is 7.34 g/cm^3/7.41 g/cm^3, respectively. Density value of SPS-30 magnet is relatively in substance equivalent to that of theoretical density (7.60 g/cm^3). The difference of density values between SPS-10 and SPS-20 is due to lack of enough liquid phase in the magnets, which has a better agreement with the results of Fig. 5(a) and Fig. 5(b) [22]. Obvious contrast can be seen between flake and neighbor boundary among Fig. 6(c), Fig. 6(e), Fig. 6(d) and Fig. 6(f). This contrast also indicates the inhomogeneous distribution of each RE element. The bright regions are composed of abundant RE element in the boundary. One reason is that RE-rich phases are extruded into boundary with compressive pressure process [23].

Compared with SPS-10 magnet, thickness of the RE-phase layer generally diminishes in SPS-20 magnets. Besides, the RE-rich phases become smoother. This is beneficial in weakening the exchange coupling between adjacent grains [24]. It is worthy to note that the reduction of nonmagnetic RE-rich phase contributes to the enhance-
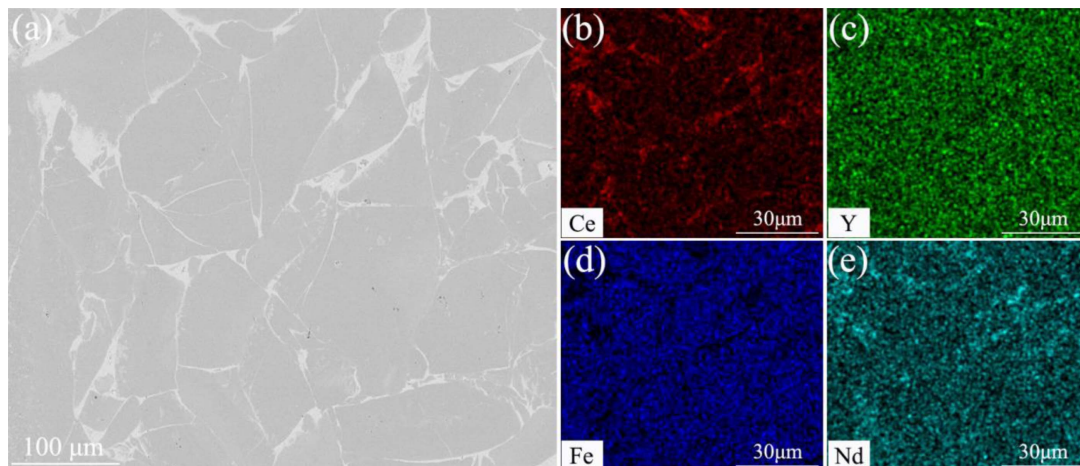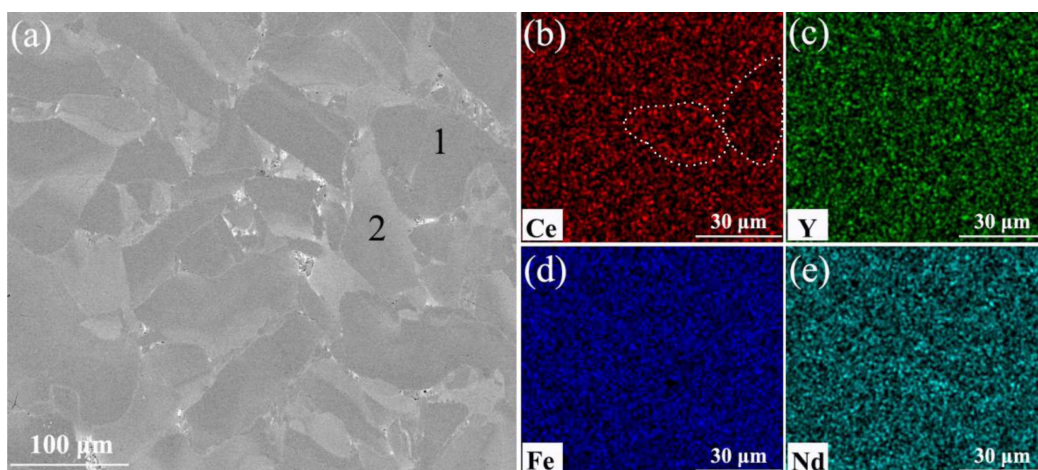
Fig. 7. (Color online) (a) BSE image and EDS elemental mappings of (b) Ce, (c) Y, (d) Fe and (e) Nd for SPS-10 magnets.

ment of J_r and $(BH)_{max}$ as well.

Ce, Y and Nd rare earth elements easily infiltrate into 2:14:1 tetragonal crystal cell. Nonetheless, their metallurgical distribution behavior and efficiency may be quite different during preparing process. Fig. 7 shows the EDS results and BSE image of SPS-10 magnet. According to the EDS mapping results in Fig. 7(b)-(e), the RE-rich phase consisted of Ce-rich and Nd-rich rather than Fe-rich compounds. The mapping shows a uniform contrast for Y element, which is different from that of Ce element. Inhomogeneous distributions suggest that all of RE elements joint to diffuse into each compound during the liquid phase sintering process[8]. Agglomerated RE-rich phase is usually reduced at the uneven triple junctions. This situation has been observed in the (Ce, Nd)-Fe-B sintered magnet. Simultaneously, similar phenomena of homogeneous RE-rich phase and less CeFe$_2$ phase have been previously investigated by Yan *et al.* [25].

Unlike Nd/Ce element, Y element shows different metallurgical behavior and Y prefers to infiltrate in 2:14:1 main phases, which may have a favorable effect on the stability of the main phases [9]. Continuously, BSE image and EDS elemental mappings of SPS-20 magnet are shown in Fig. 8. Based on EDS results, No. 1 spot marked in Fig. 8(a) exhibits the region of the Ce-lean main phase, whereas, No. 2 spot exhibits the Ce-rich region. What's more, Ce mapping results show different distributions as clearly distinguished in Fig. 8(b). Ce-lean and Ce-rich areas coexist in main phases of SPS-20 magnet. Comparably, Y and Nd elements in main phases are uniformly distributed in Fig. 8(c) and Fig. 8(e). Consequently, this behavior has the advantage of substantial remanence and coercivity enhancement.

Much more ways are adopted to explain the abnormal value of magnetic properties of SPS-20 magnet. Grain morphology and element distributions of matrix grains

Fig. 8. (Color online) (a) BSE graph and EDS elemental mappings of (b) Ce, (c) Y, (d) Fe and (e) Nd for SPS-20 magnets.
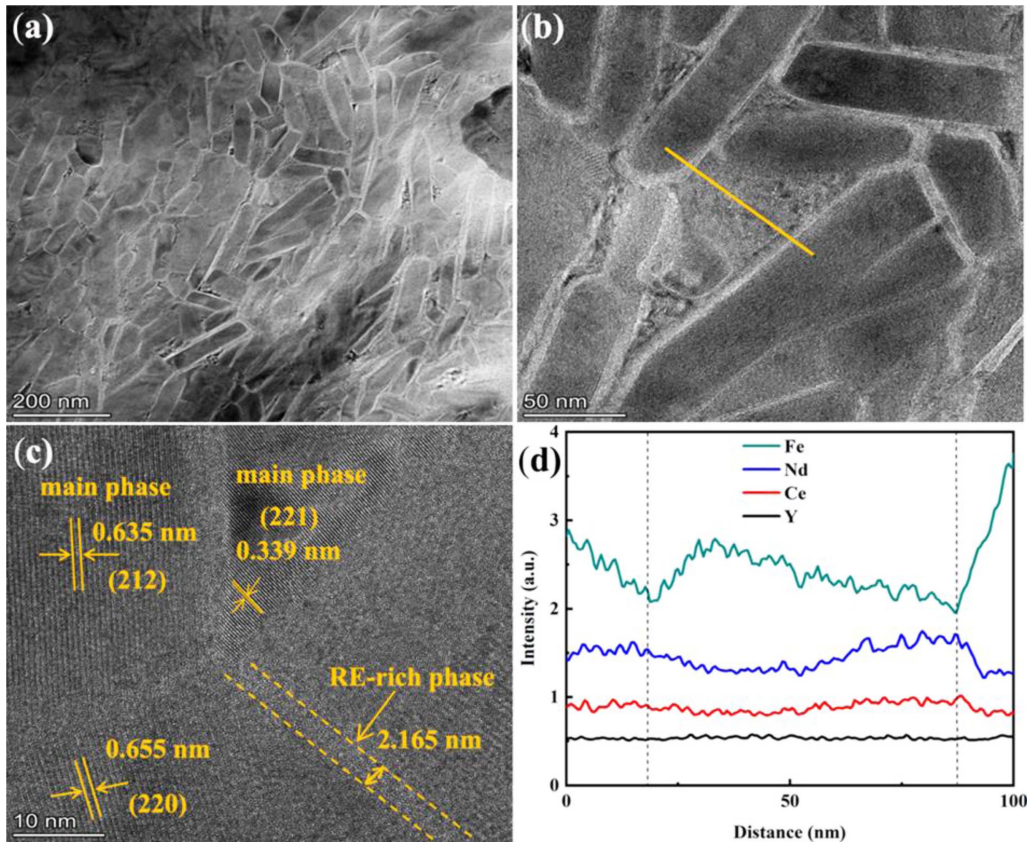
Fig. 9. (Color online) (a, b) TEM micrographs of SPS-20 magnets, (c) HRTEM micrograph of main phase/RE-rich phase and (d) EDS result along the yellow line marked in (b).

and peripheries are studied by TEM in detail. In Fig. 9(a), after undergoing densification, framework of grains in SPS-20 magnet is going to become platelet-shape. Its average length is about 132 nm and average width is about 37 nm. This phenomena intimates that different morphology of 2:14:1 phase is accordingly ascribed to preparing process [26, 27]. In nanocrystalline Nd-Fe-B ribbons, equiaxed grains prepared by rapid solidification procedure are usually observed [28]. Nevertheless, non-equilibrium SPS process leads to grain prolongs along one direction and anisotropic grains will be derived. Compared with the grain growth direction perpendicular to the c-axis, the grain growth along the c-axis direction turns out to be slower when the epitaxial dynamic energy can expand to the (*00l*) plane of the 2:14:1 main phase grains in direct contact with layer structures [29]. Hence, the grain morphology of SPS-20 magnet are mainly composed of elongated grains. Similar microstructures have also been reported by Huang *et al*. [24].

TEM micrograph / EDS results are displayed in Fig. 9(b)/Fig. 9(d). The results reveal that Nd and Ce are rich in grain boundary (GB) while Y is uniformly distributed in main phases. This sufficient explanation can also viewed

in Fig. 7 and Fig. 8. The microstructural information of main phases and boundary distance between adjacent grains in Fig. 9(c) are depicted with High Resolution Transmission Electron Microscope (HRTEM). Elongated grains have been gained. It is helpful for higher J_r and $(BH)_{max}$. Thickness of grain boundary (GB) layer is about 2.165 nm. The value is approximate to the length of exchange coupling (2-3 nm, calculated by $\pi\sqrt{A/K}$, where A represents exchange coefficient, K represents magneto-crystalline anisotropy constant) [30, 31].

The thickness of GB layer plays an essential role on demagnetization coupling effect and makes coercivity increasing effectively. These advantages concomitantly coincide well with the novel overall magnetic properties of Nd-20 ribbons and SPS-20 permanent magnets manifested in Fig. 2(a), Fig. 2(b) and Fig. 3(b), respectively.

4. Conclusions

Evolution of the thermal stability, microstructure and metallurgical behavior of the SPSed magnets was systematically studied. Main conclusions are given below.

(1) For $x \geq 20$, the occurrence of $CeFe_2$-type phases in

the $(Y_{50}Ce_{50})_{30-x}Nd_xFe_{68.9}B_{1.1}$ ribbons and SPSed magnets can be suppressed.

(2) Metallurgical distribution behavior of the RE elements shows that the rare earth elements are extruded to the boundary during the sintering process. Then liquid RE phases are extruded into the voids and dense SPS-20 magnet is finally gained.

(3) Measured Curie temperature of magnet is higher than the theoretical value due to different distribution behavior of Y and Ce, so that temperature stability of Ce-containing magnets can be further improved.

(4) HRTEM shows that main phase grains are mainly consisted of elongated grains in SPS-20 magnet. Besides, both Nd/Ce/Y distribution efficiency and the thinner GB layer contribute to the enhanced overall magnetic properties.

Acknowledgements

References

[1] A. Trench and J. P. Sykes, Eng. **6**, 115 (2020).

[2] J. M. D. Coey, Eng. **6**, 119 (2020).

[3] S. Sugimoto, J. Phys. D: Appl. Phys. **44**, 064001 (2011).

[4] O. Gutfleisch, M. A. Willard, E. Bruck, C. H. Chen, S. G. Sankar, and J. P. Liu, Adv. Mater. **23**, 821 (2011).

[5] A. K. Pathak, M. Khan, K. A. J. Gschneidner, R. W. Mccallum, L. Zhou, K. Sun, K. W. Dennis, C. Zhou, F. E. Pinkerton, M. J. Kramer, and V. K. Pecharsky, J. Adv. Mater. **27**, 2663 (2015).

[6] W. Tang, S. Zhou, and R. Wang, J. Appl. Phys. **65**, 3142 (1989).

[7] J. F. Herbst, Rev. Mod. Phys. **63**, 819 (1991).

[8] X. Fan, G. Ding, K. Chen, S. Guo, C. You, R. Chen, D. Lee, and A.Yan, Acta Mater. **154**, 343 (2018).

[9] X. Liao, J. Zhang, H. Yu, X. Zhong, A. J. Khan, X. Zhou, H. Zhang, and Z. Liu, J. Mater. Sci. **54**, 14577 (2019).

[10] J. Liu, H. SepehriAmin, T. Ohkubo, K. Hioki, A. Hattori, T. Schrefl, and K. Hono, Acta Mater. **82**, 336 (2015).

[11] H. Wuest, L. Bommer, T. Weissgaerber, and B. Kieback, J. Magn. Magn. Mater. **392**, 74 (2015).

[12] Y. Huang, Z. Li, X. Ge, Z. Shi, Y. Hou, G. Wang, Z. Liu, and Z. Zhong, J. Magn. Magn. Mater. **399**, 175 (2016).

[13] T. Tomse, J. Jacimovic, L. Herrmann, F. Greuter, R. Simon, S. Tekavec, J. M. Dubois, and S. Kobe, J. Alloys Compd. **744**, 132 (2018).

[14] S. Grasso, E. Y. Kim, T. Saunders, M. Yu, A. Tudball, S. H. Choi, and M. Reece, Cryst. Growth Des. **16**, 2317 (2016).

[15] F. Wang, J. Han, Y. Zhang, S. Liu, J. Yang, Y. Yang, A Sun, F. Yang, and R. Song, J. Magn. Magn. Mater. **360**, 48 (2014).

[16] X. Tang, R. Chen, W. Yin, C. Jin, D. Lee, and A. Yan, Appl. Phys. Lett. **107**, 202403 (2015).

[17] Y. Ma, Q. Yang, X. Chen, Y. He, W. Xiang, J. Lai, B. Shao, D. Guo, D. Chen, and K. Li, J. Rare Earths **39**, 689 (2021).

[18] T. Schrefl, J. Fidler, and H. Kronmuller, Phys. Rev. B **49**, 6100 (1994).

[19] A. V. Morozkin, Y. D. Seropegin, A. V. Gribanov, and J. M. Barakatova, J. Alloys Compd. **256**, 175 (1997).

[20] J. Déportes, D. Givord, K. R. and A. Ziebeck, J. Appl. Phys. **52**, 2074 (1981).

[21] A. H. Sepehri, L. Liu, T. Ohkubo, M. Yano, T. Shoji, A. Kato, T. Schrefl, and K. Hono, Acta Mater. **99**, 297 (2015).

[22] J. Liu, A. H. Sepehri, T. Ohkubo, K. Hioki, A. Hattori, T. Schrefl, and K. Hono, Acta Mater. **61**, 5387 (2013).

[23] T. Akiya, J. Liu, A. H. Sepehri, T. Ohkubo, K. Hioki, A. Hattori, and K. Hono, Scripta Mater. **81**, 48 (2014).

[24] Y. Huang, Z. Li, X. Ge, Z. Shi, Y. Hou, G. Wang, Z. Liu, and Z. Zhong, J. Alloys Compd. **797**, 1133 (2019).

[25] C. Yan, S. Guo, R. Chen, D. Lee, and A. Yan, IEEE. Trans. Magn. **50**, 2102605 (2014).

[26] S. Rehman, Q. Jiang, L. He, H. Xiong, K. Liu, L. Wang, M. Yang, and Z. Zhong, Phys. Lett. A **383**, 125878 (2019).

[27] Y. Hou, Y. Wang, Y. Huang, Y. Wang, S. Li, S. Ma, Z. Liu, D. Zeng, L. Zhao, and Z. Zhong, Acta Mater. **115**, 385 (2016).

[28] R. Coehoorn, and J. Duchateau, Mater. Sci. Eng. **99**, 131 (1988).

[29] T. G. Woodcock, and O. Gutfleisch, Acta Mater. **59**, 1026 (2011).

[30] H. Kronmuller, R. Fischer, M. Seeger, and A. Zern, J. Phys. D: Appl. Phys. **29**, 2274 (1996).

[31] A. H. Sepehri, T. Ohkubo, T. Shima, and K. Hono, Acta Mater. **60**, 819 (2012).